Malitckii, E.; Yagodzinskyy, Y.; Lehto, P.; Remes, H.; Romu, J.; Hänninen, H.

Hydrogen effects on mechanical properties of 18% Cr ferritic stainless steel

Published in:
Materials Science and Engineering A: Structural Materials: Properties, Microstructures and Processing

DOI:
10.1016/j.msea.2017.06.028

Published: 08/06/2017

Document Version
Peer-reviewed accepted author manuscript, also known as Final accepted manuscript or Post-print

Hydrogen effects on mechanical properties of 18%Cr ferritic stainless steel

E. Malitckii, Y. Yagodzinskyy, P. Lehto, H. Remes, J. Romu and H. Hänninen,

Aalto University School of Engineering, Espoo, Finland

Abstract

Role of microstructure in susceptibility of 18Cr ferritic stainless steel to hydrogen embrittlement was studied. Specimens of the studied steel were charged with hydrogen electrochemically from 0.1N H_2SO_4 solution under controlled cathodic potential providing a homogeneous hydrogen distribution over the specimen cross-sections. Thermal desorption spectroscopy analyses were carried out investigating the uptake, trapping and diffusion of hydrogen in the ferritic stainless steel.

Microstructural change caused by heat-treatment at 1050°C and 1200°C associated preferably with grain size growth from 18 μm to 65 μm and 349 μm, respectively, resulting in significant degradation of the mechanical properties of the studied steel. The effect of the grain size growth on hydrogen susceptibility was studied with constant extension rate test (CERT) performed under continuous hydrogen charging. It is found that hydrogen has a remarkable effect on the elongation to fracture of the Fe-Cr ferrite: in the presence of H elongation to fracture of the steel reduces up to 75% compared to the H-free counterpart. In general, the hydrogen sensitivity of the mechanical properties increases with increase of the mean grain size of the studied ferritic stainless steel. However, the detailed analysis reveals a complicated, non-linear behavior of the hydrogen sensitivity. Scanning electron microscopy (SEM) of the fracture surfaces of the tensile specimens tested during continuous hydrogen charging reveals a quasi-cleavage fracture surface morphology. Hydrogen-induced cracking in the studied 18Cr ferritic steel was studied using electron backscatter diffraction (EBSD) analysis from the side surfaces of the tensile tested specimens.

Keywords: ferritic stainless steel, hydrogen embrittlement, hydrogen thermal desorption, hydrogen-induced cracking.

Introduction

Ferritic stainless steels are attractive materials for applications in oil and gas as well as in automotive and marine industries due to their enhanced corrosion resistance and relatively low price compared to the austenitic stainless steel grades. However, the microstructural features of the ferrite which has body-centered cubic (bcc) crystal lattice cause a significant loss in ductility compared to that of austenitic steels having a face-centered cubic (fcc) arrangement of atoms in the crystal lattice. Furthermore, the higher atomic diffusion rates in bcc crystal lattice structure make the ferritic stainless steels more prone to formation of second phase precipitates during heat treatment resulting in an increase of ductile-to-brittle transition temperature (DBTT) [1]. Such heat treatment accompanies, for instance, welding processes resulting in formation of a gradient of microstructures through the heat-affected zone of ferritic stainless steel welds [2]. Hydrogen trapped from both manufacturing and service environments can reduce significantly the mechanical properties of ferritic stainless steels. At the same time, the effect of microstructure of ferritic steel on its susceptibility to hydrogen embrittlement is the key question.

Different mechanisms of the hydrogen embrittlement of structural materials have been proposed. High concentration of hydrogen may contribute in Hydrogen-enhanced decohesion (HEDE) events that are usually associated with a simple sequential tensile separation of atoms when a critical crack-tip-opening displacement is reached [3, 4]. Beachem proposed hydrogen-enhanced localized plasticity (HELP) mechanism which is based on the assumption that hydrogen localized near crack tips due to hydrostatic stress or entry of hydrogen at crack tips facilitates dislocation activity and localization of plastic deformation near crack tips [5]. Hydrogen embrittlement may also be primarily the result of a high concentration of vacancies ahead of the crack tip caused by hydrogen-enhanced stress-induced vacancy (HESIV) formation [6]. The proposed mechanisms of hydrogen embrittlement are used to describe the mechanism of quasi-cleavage fracture formation widely observed in the mechanical testing of hydrogen charged ferritic steels [7, 8].

Usually, the most problematic region in the ferritic stainless steel welds is the high-temperature heat-affected zone (HTHAZ). Grain coarsening and various embrittlement phenomena such us formation of martensite, 475°C, sigma phase, Laves phase and high-temperature embrittlement associated with growth of grain size and carbides/nitrides [9-14] cause a significant reduction of mechanical and corrosion properties of the ferritic stainless steels. Use of the stabilizing elements and relevant heat treatment procedures can improve substantially the weldability of the ferritic stainless steels. However, the grain size in HTHAZ can easily grow beyond 200 μm at temperatures over 1100°C [14].

At the same time, the microstructural changes such as ferrite decomposition and secondary phase precipitation associated with welding procedures, especially in HTHAZ, can make the material prone to hydrogen embrittlement. The present study aims to clarify the role of microstructure, in particular grain coarsening, in susceptibility of the ferritic stainless steel to hydrogen-induced cracking.

Experimental

The ferritic stainless steel (ASTM UNS S43940) was provided by Outokumpu Stainless Oyj in the shape of hot-rolled plate with a thickness of 3 mm. The chemical composition of the steel is shown in Table 1.

Table 1. Chemical composition of ASTM UNS S43940 ferritic stainless steel, wt%.

C	Sl	Mn	P	Cr	Mo	Nb	Ni	Ti	Cu	Al	As	Co	Sn	V	W
0,014	0,61	0,42	0,03	17,7	0,024	0,393	0,18	0,138	0,118	0,025	0,007	0,0183	0,007	0,055	0,037

Tensile specimens with a gauge length of about 32×5×1 mm were cut in transverse direction to the rolling plane. In order to increase the average grain size (GS) of the steel the prepared specimens were annealed at 1050ºC and 1200ºC for 1 h and quenched in water. All the specimens were mechanically polished finishing with 6 µm diamond paste. Marble`s reagent was used for etching of the steel. GS measurements were performed from optical microscopy photographs obtained normal to the transverse direction (from the side surface of the specimens) using the intercept length method [15].

Electrochemical hydrogen charging was performed from 0.1N H_2SO_4 solution with 20 mg/l of thiourea ($CS(NH_2)_2$) at controlled potential of -1.2 $V_{Hg/Hg2SO4}$. Thermal desorption spectroscopy (TDS) was performed with a heating rate of 6 K/min from room temperature to 850ºC. Basic pressure of ultra-high vacuum (UHV) chamber of TDS apparatus is 10^{-8} mbar. Hydrogen gas pressure was measured in UHV chamber by mass spectrometry during liner heating of the studied steel specimens. Hydrogen gas pressure was recalculated to the hydrogen desorption rate in at.ppm per second using a calibration procedure. Hydrogen concentration in the specimen was calculated as the area under the hydrogen desorption rate curve vs. time of measurement. The size of the TDS specimens is about 7.5×3.8×0.8 mm. Dwelling time between the end of electrochemical hydrogen charging and launching of the TDS measurement is about 30 min.

Tensile specimens were pre-charged with hydrogen for 4 h before tensile testing. The charging time was found to be enough for a homogeneous hydrogen distribution. Tensile tests were performed during continuous hydrogen charging using a 35 kN MTS desk-top testing machine at a strain rate of 10^{-4} s^{-1}. Tensile tests were performed at room temperature in H-free condition and during continuous hydrogen charging.

Fracture surfaces of the tested tensile specimens were studied using scanning electron microscope Zeiss Ultra 55 FEG-SEM. Microstructure was studied from the interiors of the tensile tested specimens by electron backscatter diffraction (EBSD) analysis.

Results

Annealing of the tensile specimens of the studied ferritic stainless steel results in an increase of the average GS from 18 µm for as-supplied steel to 65 µm and 349 µm for specimens heat treated at 1050ºC and 1200ºC, respectively. A relative grain size dispersion value was calculated from the measured distribution as follows [16]:

$$\frac{\Delta d}{d} = \frac{d_{max} - d_{min}}{d} = \frac{P_{99\%} - P_{1\%}}{d}, \quad (1)$$

where d is the average GS, d_{max} and d_{min} are maximum and minimum grain sizes which were replaced by the 99% and 1% probability level grain sizes, respectively. The relative dispersion parameter calculated for as-supplied condition of the studied steel was found to be about 2.8. After heat treatment of the studied steel at 1050ºC a minor increase of the relative dispersion value of the GS distribution was observed to the value of about 2.9. However, the dispersion increases significantly up to 4.6 with the increase of annealing temperature to 1200ºC.

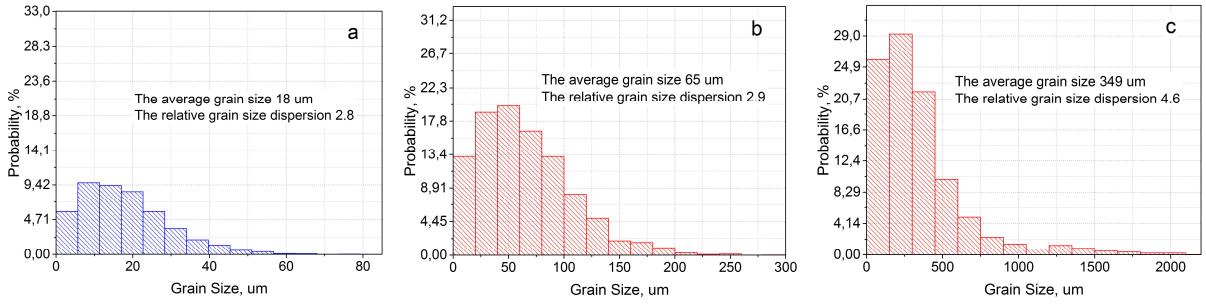

Figure 1. GS distribution of the studied ferritic stainless steel measured in as-supplied (a) condition and after annealing at 1050°C (b) and 1200°C (c) for 1 h.

Constant extension rate tests (CERT) of the studied ferritic stainless steel were performed first in H-free condition for as-supplied and annealed steel specimens. The obtained CERT stress-strain curves are shown in Fig. 2. The annealing procedures of the as-supplied steel specimens resulting in the increase of the average GS affect significantly the mechanical properties. The elongation to fracture of about 29.3% obtained for as-supplied steel specimen reduces to about 27.5% and 15.7% with the increase of the average grain size to 65 µm and 349 µm, respectively. Tensile strength tends also to decrease from 428 MPa to 395 MPA and 368 MPa, respectively.

While the elongation to fracture and tensile strength parameters manifest a uniform degradation of the mechanical properties of the ferritic stainless steel, the effect of GS coarsening on yield stress parameters is more complicated. The yield stress of the steel specimens tested in the as-supplied condition is about 300 MPa and it reduces to about 237 MPa with the increase of the average GS to 65 µm. Following coarsening of the grain structure of the studied steel causes an increase of the yield stress that is in contrast with Hall-Petch relationship [17, 18]. The observed discrepancy is discussed later.

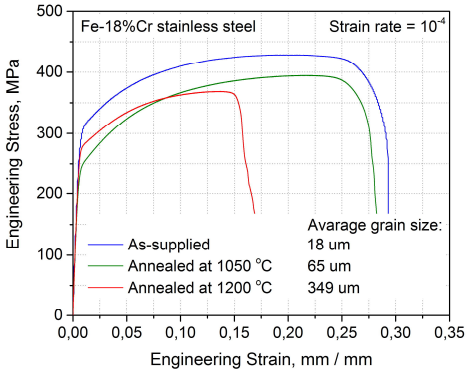

Figure 2. CERT stress-strain curves of as-supplied and annealed specimens of ASTM UNS S43940 ferritic stainless steel obtained in air with strain rate of 10^{-4} s^{-1}.

Hydrogen detrapping and release from the ASTM UNS S43940 ferritic stainless steel specimens were studied using a TDS apparatus after electrochemical hydrogen charging for 1, 2, 4 and 18.5 h. As shown in Fig. 3 the hydrogen content increases rapidly with time of H-charging from 1 to 4 h and reaches the value of about 100 at.ppm. Continuing hydrogen charging results in almost the same value of the hydrogen concentration measured from the ferritic stainless steel specimens evidencing that the electrochemical hydrogen charging during 4 h or more at the conditions described above is associated with the homogeneous hydrogen distribution through the specimen thickness.

Diffusion flux and concentration gradient of interstitial solute atoms at some particular point of the metallic material matrix x are controlled by the diffusion process and varies with the square root of time [19]:

$$x = \alpha\sqrt{Dt}, \tag{2}$$

where α is a constant and depends on the concentration gradient of the solute atoms at a particular point of the matrix. Since the specimen with characteristic thickness of about 0.8 mm reaches a hydrogen saturation state after electrochemical hydrogen charging for 4 h at temperature of about 20°C, the effective diffusion coefficient of hydrogen can be estimated [20] to be about 4.3×10^{-11} m^2 s^{-1}.

Solving the corresponding boundary problem for diffusion equation an expression for the hydrogen concentration profile can be obtained [21]:

$$C(x) = \frac{4C_0}{\pi}\sum_{n=0}^{\infty}\frac{(-1)^n}{(2n+1)}\cos\frac{(2n+1)\pi x}{h}\left(1 - e^{-\frac{\pi^2(2n+1)^2 D(T_s)t_s}{h^2}}\right)e^{-\frac{\pi^2(2n+1)^2 D(T_d)t_d}{h^2}}, \tag{3}$$

where C_o is the concentration of hydrogen on the surface, t_s and T_s are time and temperature of hydrogen charging, t_d and T_d are time and temperature of hydrogen desorption, respectively, h is the thickness of the specimen, and D is the diffusion coefficient.

Hydrogen concentration profile after electrochemical hydrogen charging of 0.8 mm thick ASTM UNS S43940 stainless steel plate for 4 h and dwelling at room temperature for 30 min required for launching of TDS measurement is shown in Fig. 4. The same equation was solved to estimate the total hydrogen concentration profile in the studied

steel directly after electrochemical hydrogen charging. The total concentration of hydrogen at the final stage of the H-charging procedure was estimated to be about 290 at.ppm that is about three times higher than the measured value. The area between the hydrogen concentration profiles shown in Fig. 4 corresponds to the amount of hydrogen escaped from the specimen during the dwell time required for measurement process.

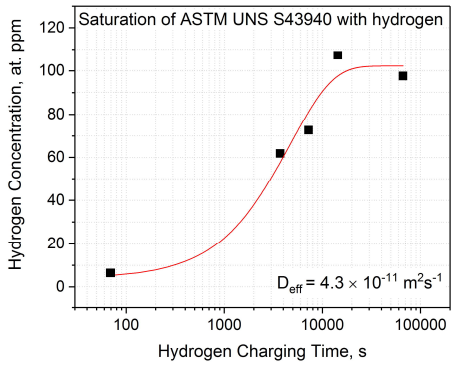

Figure 3. Relationship between hydrogen charging time and measured hydrogen concentration in the ASTM UNS S43940 ferritic stainless steel.

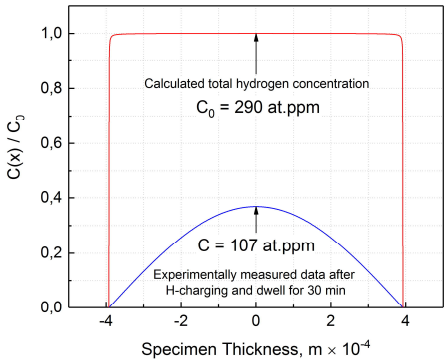

Figure 4. Hydrogen concentration profile after electrochemical hydrogen charging of 1 mm thick ASTM UNS S43940 ferritic stainless steel plate for 4 h and dwelling at room temperature for 30 min (blue) compared to calculated total hydrogen concentration without dwelling (red).

The electrochemical hydrogen charging affects markedly the mechanical properties of ASTM UNS S43940 stainless steel as shown in Fig. 5. Obtained CERT results manifest a significant reduction of elongation to fracture and an increase of yield stress in all the specimen grain sizes. The parameters of the mechanical properties are summarized in Table 2.

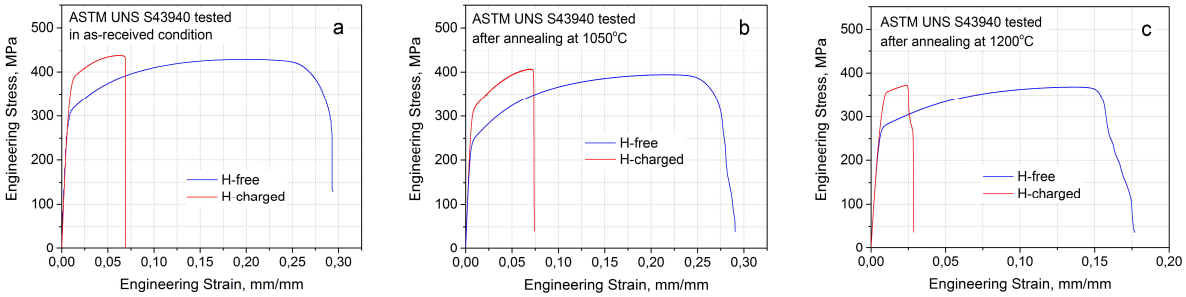

Figure 5. CERT stress-strain curves of H-free and H-charged ASTM UNS S43940 ferritic stainless steel specimens with average GS of about 18 μm (a), 65 μm (b) and 349 μm (c).

Table 2. Hydrogen effect on the CERT parameters of the tensile specimens of ASTM UNS S43940 ferritic stainless steel.

GS, μm	$\frac{R_{p0,2}, MPa}{R_{p0,2H}, MPa}$	$\frac{R_m, MPa}{R_{mH}, MPa}$	$\frac{\varepsilon, \%}{\varepsilon_H, \%}$
18	$\frac{300}{371}$	$\frac{428}{437}$	$\frac{29.3}{6.9}$
65	$\frac{237}{311}$	$\frac{395}{406}$	$\frac{27.5}{7.3}$
349	$\frac{274}{350}$	$\frac{368}{372}$	$\frac{15.7}{2.5}$

The parameter of sensitivity to hydrogen is defined as:

$$\delta_H = (x - x_H)/x, \quad (4)$$

where x and x_H are CERT parameters obtained after tensile testing of H-free and H-charged tensile specimens of the studied steel. The dependence of the average GS on parameter of sensitivity to hydrogen is shown in Fig. 6. The results are divided to Stage I and Stage II according to the average GS growth from 18 μm to 65 μm and from 65 μm to 349 μm, respectively. In general, the sensitivity to hydrogen of elongation to fracture and yield stress increase with growth

of the average GS of the studied steel. However, the detailed analysis of the results manifests a minor decrease of the deleterious effect of hydrogen on elongation to fracture at Stage I and a significant increase at Stage II of the graph. For yield stress the opposite effect was observed. Only a minor effect of hydrogen on tensile strength was observed remaining almost the same at Stage I and Stage II. Such a behavior is caused apparently by microstructural change associated with ferrite decomposition and/or secondary phase precipitation in the studied steel during the heat treatment.

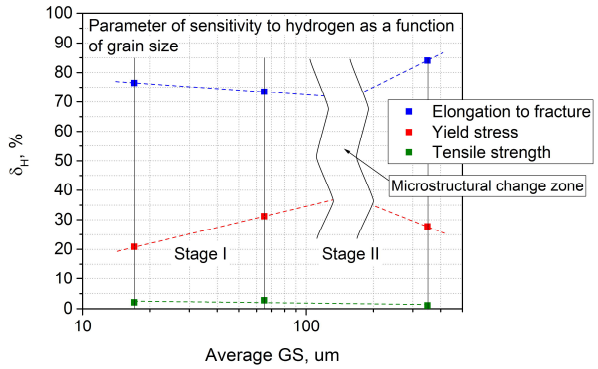

Figure 6. Sensitivity to hydrogen parameter as a function of average GS of the ASTM UNS S43940 ferritic stainless steel.

Fully ductile dimpled fracture surface was observed in the steel specimens with average GS of about 18 µm and 65 µm tested in hydrogen-free condition as shown in Fig. 7a. The dimples contain none-metallic inclusions (NMI) of Ti/Al oxides and Nb carbides. Fracture surface of the tensile test specimens with an average GS of about 349 µm exhibits a more complicated fracture behavior. Both ductile dimpled fracture surface and cleavage facets were observed as shown in Fig. 7b, c.

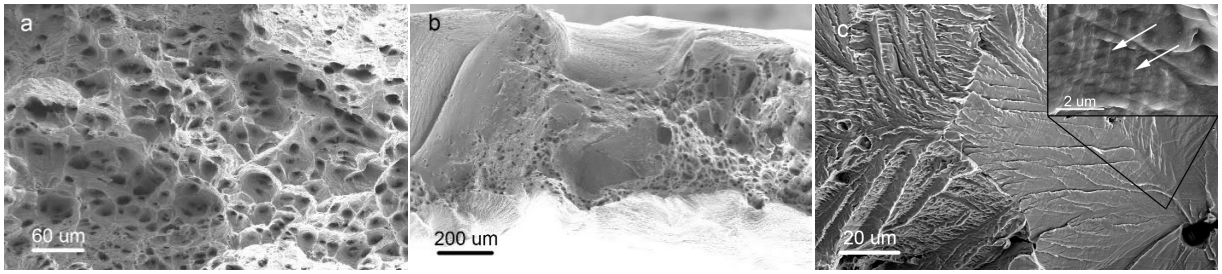

Figure 7. Fractographs of the fracture surfaces obtained in CERT of hydrogen-free ASTM UNS S43940 ferritic stainless steel specimens tensile tested in as-supplied condition (a) and after annealing at 1200°C (b) and higher magnification of the specimen fracture surface tested after annealing at 1200°C (c).

The cleavage crack initiates at Al-oxide particles and propagates through the grain or a few neighboring grains. The "river pattern" running from a NMI to the grain boundaries was observed. At the same time, a regular fine structure formed normal to the crack path probably due to the relaxation of the dislocation structure present on the crack wake of the cleavage facets as shown by arrows in insert of Fig. 7c.

Electrochemical hydrogen charging of the studied steel results in a remarkable change of the fracture surface morphology. Fracture surfaces of the steel specimens with average GS of about 18 µm and 65 µm are mainly transgranular accompanied with some areas of intergranular fracture shown by dashed line in Fig. 8a. The areas of intergranular fracture are randomly distributed on the fracture surface of the steel specimens with average GS of about 18 µm, while in the steel specimens with average GS of about 65 µm the intergranular fracture areas are localized at the corners of the fracture surface. Further coarsening of the grain structure results in the formation of fully transgranular fracture surface after tensile testing during continuous hydrogen charging as shown in Fig. 8c. The fine structure (see insert of Fig. 8b) is produced probably by relaxation of the dislocation structure of the crack wake in the vicinity of the propagating crack. These fine structures were observed in all the studied steel grain sizes tested during continuous hydrogen charging. NMIs play obviously an important role in the transgranular cleavage crack initiation, since "river pattern" is always observed running from NMIs.

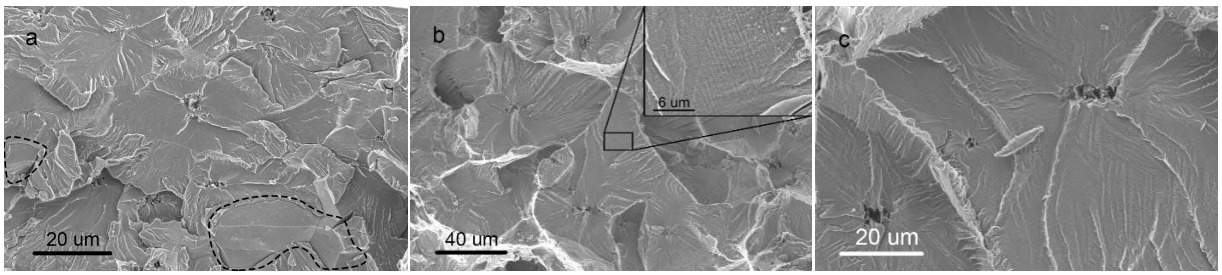

Figure 8. Fractographs of the fracture surfaces obtained in CERT of ASTM UNS S43940 ferritic stainless steel specimens with average GS of about 18 µm (a), 65 µm (b) and 349 µm (c) tested during continuous hydrogen charging.

Fractographs obtained with higher magnification (see Fig. 9a, b) show a well-defined "stairs-like" structure formed in the vicinity of the NMIs. Worth to note is that the fine "stairs-like" structure was observed only in the steel specimens with average GS of about 65 µm and 349 µm. The "river pattern" widely observed on the fracture surfaces of the steel specimens shows also a "stairs-like" structure forming on the facet side of the steps as shown in Fig. 9c.

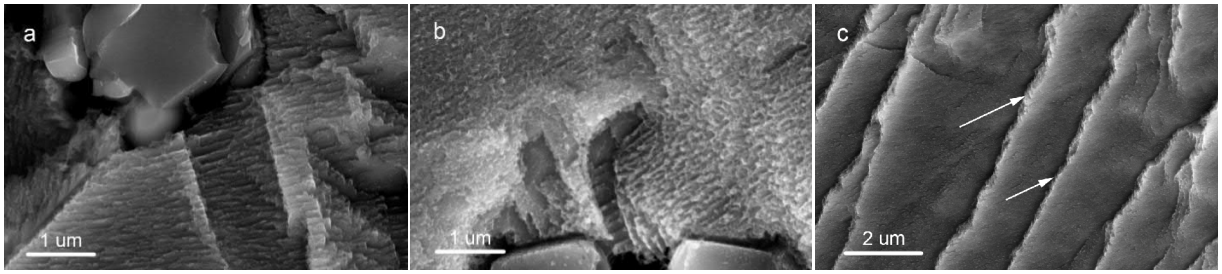

Figure 9. Detail of fracture surface obtained in CERT of ASTM UNS S43940 ferritic stainless steel specimens with average GS of about 65 µm (a, c) and 349 µm (b) tested during continuous hydrogen charging.

Typical EBSD maps of the side surface of the as-supplied steel specimens obtained after CERT performed in H-free and H-charged conditions are shown in Fig. 10a, b. The microstructure of the specimens tested in H-free condition comprises elongated grains along the loading direction. The grains are free of twins and deformed plastically due to the dislocation slip only. The EBSD map of the side surface of the specimens tested in CERT during continuous hydrogen charging shown in Fig. 10b exhibits the transgranular character of hydrogen-induced crack propagation in ASTM UNS S43940 ferritic stainless steel. The microstructure of the specimen tested during hydrogen charging contains significantly smaller amount of plastic deformation compared to that in H-free specimens. The deformation is localized mainly in the vicinity of the cracks widely observed on the side surface of the as-supplied steel specimens tested during continuous hydrogen charging. The microstructural morphology of the side surfaces of the steel specimens with different average GS remains almost the same. However, the density of the cracks observed on the side surface of H-charged specimens decreases with the increase of the average GS of the studied steel.

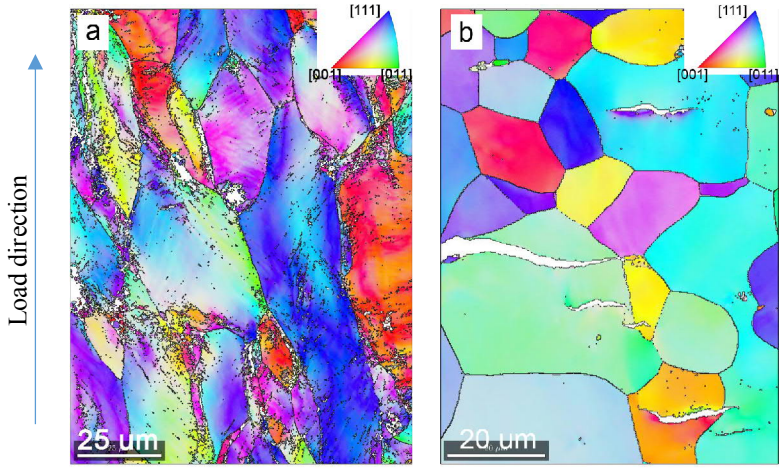

Figure 10. EBSD maps of the side surfaces obtained in CERT of as-supplied ASTM UNS S43940 ferritic stainless steel specimens with average GS of about 18 µm tested in hydrogen-free condition (a) and during continuous hydrogen charging (b).

Subtle deformation structures formed during mechanical testing were studied using the local misorientation analysis (Kernel Average Misorientation) of the side surfaces of the studied ferritic steel specimens tested during continuous hydrogen charging. The strain was found to be highly localized in the vicinity of the crack tips forming deformation structures associated with dislocation slip as shown in Fig. 11. Cracks propagate obviously through the observed slip bands forming the quasi-cleavage step-wise fracture surface. The analysis of the crystal orientation of the individual grains containing cracks that manifest the observed slip band structures are in good agreement with slip plane of type {110}, which is the preferable slip plane in bcc crystal lattice [19].

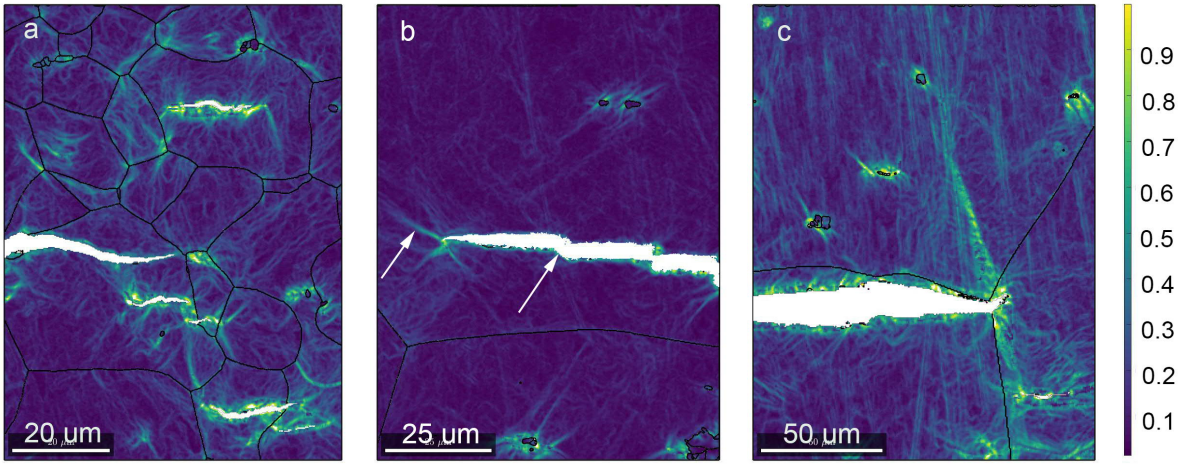

Figure 11. Kernel average misorientation maps of ASTM UNS S43940 ferritic stainless steel from side surface of the steel specimens with average GS of about 18 µm (a), 65 µm (b) and 349 µm (c) after CERT during continuous hydrogen charging.

Discussion

CERT testing of the studied ASTM UNS S43940 ferritic stainless steel specimens in as-supplied condition and after annealing causing an increase of the average GS shows contradictory results. The yield stress was found to increase with an increase of the average GS from 65 µm to 349 µm that does not follow the Hall-Petch relationship [17, 18]. Such a behavior is caused apparently by precipitation hardening which results from the presence of second-phase precipitates in the matrix that inhibit dislocation movement through the crystal [19]. At the same time, the brittle inclusions/precipitates can be responsible for the nucleation of the cleavage crack [19, 22] causing the formation of the brittle transgranular fracture observed in the steel specimen with average GS of about 349 µm as shown in Fig. 7b, c. However, the microscopy of the studied steel does not reveal any changes in the precipitate density with the increase of the annealing temperature from 1050ºC to 1200ºC. Decomposition of ferrite and formation of chromium-rich nano-scale clusters is also a possible reason of the steel hardening. Chromium-rich cluster formation occurs by spinodal decomposition of ferrite to iron-rich α- and chromium-rich ά- phases [10, 11]. Also, in characterisation of local GS variation of a welded steel the increase of relative grain size dispersion in heat-affected zone was attributed to decomposition of the weld metal and second-phase formation that correlates well with the obtained results [23, 24].

The diffusivity of hydrogen in α-iron is relatively high even at room temperature [25]. However, the diffusivity of hydrogen in Fe-alloys decreases with the increase of the concentration of alloying elements due to hydrogen trapping at defects/crystal imperfections caused by interstitial and substitutional atoms as well as second-phase precipitates [26-28]. Hydrogen concentration associated with a homogeneous hydrogen distribution through the specimen thickness measured to be about 100 at.ppm is attributed mainly to trapped hydrogen. Difference between measured hydrogen concentration and the calculated hydrogen concentration at the final stage of the hydrogen charging defines apparently the so-called diffusing hydrogen locating preferably at the tetrahedral positions of the BCC crystal lattice as well as at the other trapping sites of low activation energies [29].

In general, the deleterious effect of hydrogen on the mechanical properties of the studied steel increases with the increase of the average GS as shown in Fig. 6a. The detailed examination reveals, however, a reduction of the sensitivity to hydrogen of elongation to fracture in steel specimens with average GS of about 65 µm. Increase of the sensitivity to hydrogen of elongation to fracture of steel specimens with GS of about 349 µm is associated probably with a synergistic effect of both hydrogen and decomposition of the ferrite. The opposite effect was observed for yield

stress. If the relative grain size dispersion parameter is associated with ferrite decomposition and/or secondary phase formation in the studied steel, its change affects apparently the parameter of the sensitivity to hydrogen. According to Fig. 6, one can conclude that hydrogen sensitivity of the studied steel depends mainly on microstructural features associated with ferrite decomposition and secondary phase formation rather than with GS growth.

The hydrogen-induced transgranular cracks widely observed in the steel specimens with different average GSs is apparently quasi-cleavage fracture, which nucleates at NMIs and propagates through the crystal. Lines of the "river pattern" run approximately parallel to the crack propagation direction [30, 31]. According to the EBSD observations shown in Fig. 10 and Fig. 11 one can conclude that hydrogen results in a significant localisation of the plastic strain in the vicinity of the crack tips forming deformation structures associated with slip bands. This observation is consistent with HELP mechanism [5]. The cracks propagate obviously through the observed localized strain zones in all studied steel grain sizes.

A number of mechanisms of hydrogen-induced quasi-cleavage crack formation were proposed. One is based on the assumption that locally high total hydrogen concentration accumulates in regions of highly localized strain near the crack tips due to hydrostatic stress [32]. These concentrations may be sufficient to cause a significant reduction of the lattice cohesive strength resulting in quasi-cleavage crack propagation [7]. According to the theory proposed by Nagumo and co-workers the primary function of hydrogen in hydrogen embrittlement is the stabilisation and promotion of vacancy agglomeration [6]. Nano-voids can nucleate and grow in the presence of hydrogen in regions of highly localised stress. Thereby, nano-void coalescence mechanism was proposed by Neeraj and co-workers describing the formation of quasi-brittle fracture surfaces with "hole-joined" microstructure observed in ferritic steel [8]. Both mechanisms are possible in formation of the hydrogen-induced fracture surface obtained in CERT of the studied ferritic stainless steel. It seems that the fine "stairs-like" microstructure observed on the fracture surface in the vicinity of the NMIs forms preferably due to the reduction of the lattice cohesive strength under highly localised tensile stress after failure of the NMIs in the presence of hydrogen. As the crack propagates the "river pattern" is formed and the quasi-brittle terraces become less distinct as shown in Fig. 9c that can be caused by either nano-void coalescence or relaxation processes associated with the underlying dislocation structures [7].

Quasi-cleavage crack formation in ferritic stainless steel was observed also by Tähtinen et al. [33], where the hydrogen induced micro-twinning was suggested to be responsible for transgranular cracking. The resulting fracture was expected to occur along the twin interfaces ({110}-planes in ferritic stainless steel) or by micro-twinning ahead of the advancing crack. However, no evidence of micro-twinning was found in this study possibly due to limited resolution of the EBSD analysis. Further investigation with advanced transmission electron microscopy techniques are required.

Conclusions

The effective diffusivity of hydrogen in the ASTM UNS S43940 steel was calculated to be about 4.3×10^{-11} m^2 s^{-1} that is almost one hundred times slower as compared with pure iron [34]. Hydrogen uptake and trapping in the ferritic stainless steel were studied after electrochemical hydrogen charging at controlled potential of -1.2 $V_{Hg/Hg2SO4}$ evidencing that the total hydrogen concentration after pre-charging for 4 h is about 290 at.ppm.

Hydrogen reduces significantly the elongation to fracture of the studied steel tested in CERT during continuous hydrogen charging, and the yield stress was found to increase in the presence of hydrogen. In general, the sensitivity to hydrogen of elongation to fracture and yield stress increases with the increase of the average GS. However, the detailed analysis reveals relationship between the microstructural change and parameter of hydrogen sensitivity: the sensitivity to hydrogen of elongation to fracture increases with increase of the relative dispersion parameter associated with ferrite decomposition and/or secondary phase formation. The opposite effect of hydrogen on yield stress was observed. One can conclude that growth of the mean GS provides only minor effect on the sensitivity to hydrogen, while decomposition of ferrite and/or secondary phase formation caused by the heat-treatment can primarily result in the increase of the susceptibility to hydrogen of the studied 18Cr stainless steel.

Fracture surfaces of the steel specimens with average grain size of about 18 μm and 65 μm are mainly transgranular accompanied with some areas of intergranular fracture. Further coarsening of the grain structure results in formation of fully transgranular fracture surface after tensile testing during continuous hydrogen charging. According to the SEM/EBSD observations transgranular fracture initiates at the NMIs of Ti/Al oxide particles and propagates through the deformation structures forming a quasi-cleavage fracture surface. The orientations of the observed deformation structures correlate well with the orientations of the dislocation slip planes in BCC crystal lattice.

Acknowledgments

The ASTM UNS S43940 ferritic stainless steel was provided by Outokumpu Stainless Oyj. Research was partly supported by Aalto University.

References

1 R.A. Lula, “Toughness of ferritic stainless steels”, ASTM San Francisco, Calif. (1979).
2 H. Remes, P. Lehto, J. Romanoff, “Microstructure and strain-based fatigue life approach for high-performance welds”, Advan. Mater. Res., vol. 891-892, pp. 1500-1506 (2014).
3 A.R. Troiano, “The role of hydrogen and other interstitials on the mechanical behavior of metals”, Trans. Am. Soc. Met., vol. 53, pp. 54-80 (1960).
4 R.A. Oriani, R.H. Josephic, “Equilibrium aspects of hydrogen-induced cracking of steels”, Acta Mater., vol. 22, pp. 1065-74 (1974).
5 C.D. Beachem, “A new model for hydrogen assisted cracking (hydrogen embrittlement)”, Met. Trans., vol. 3A, pp. 437-451 (1972).
6 M. Nagumo, “Hydrogen related failure of steels – a new aspect”, Mater. Sci. Tech., vol. 20, pp. 940-50 (2004).
7 M.L. Martin, I.M. Robertson, P. Sofronis, “Interpreting hydrogen-induced fracture surfaces in terms of deformation processes: A new approach”, Acta Mater., vol. 59, pp. 3680-3687 (2011).
8 T. Neeraj, R. Srinivasan, J. Li, “Hydrogen embrittlement of ferritic steels: Observations on deformation microstructure, nanoscale dimples and failure by nanovoiding”, Acta Mater., vol. 60, pp. 5160-5171 (2012).
9 J. J. J. Zaayman, “Improvements to the toughness of the heat affected zone in welds of 11 to 12 per cent chromium steels”, Doctorate thesis supplement, University of Pretoria (1994).
10 T.J. Marrow, “The fracture mechanism in 475ºC embrittled ferritic stainless steels, Fatigue and Fracture of Engineering Materials and Structures”, Issue 19, pp. 919-933 (1996).
11 P. Hedström, F. Huyan, J. Zhou, S. Wessman, M. Thuvander, J. Odqvist, “The 475ºC embrittlement in Fe-20Cr and Fe-20Cr-X (X=Ni, Cu, Mn) alloys studied by mechanical testing and atom probe tomography”, Materials Science & Engineering, vol. A574, pp. 123-129 (2013).
12 T. Yamagishi, M. Akita, M. Nakajima, Y. Uematsu, K. Tokaji, ”Effect of σ-phase embrittlement on fatigue behavior in high chromium ferritic stainless steel”, Procedia Engineering, vol. 2, pp. 275-281 (2010).
13 M. P. Sello, W. E. Stumpf, “Laves phase embrittlement of ferritic stainless steel type AISI 441”, Mat. Sci. Eng., vol. 527, pp. 5194-5202 (2010).
14 J. C. Lippold, J. D. Kotecki, ”Welding metallurgy and weldability of stainless steels”, John Wiley & Sons, Inc., Hoboken, New Jersey (2005).
15 ATSM-E1382-97. Standard test methods for determining average grain size using semiautomatic and automatic image analysis. West Conshohocken (PA): ASTM International, (2007).
16 S. Berbenni, V. Favier, M. Berveiller, “Micro-macro modelling of the grain size distribution on the plastic flow stress of heterogeneous materials”, Comput. Mater. Sci., vol. 39, pp. 96-105 (2007).
17 E.O. Hall, “The deformation and ageing of mild steel: III Discussion of results”, Proc. Phys. Soc., vol. B64, pp. 747-53 (1951).
18 N.J. Petch, “The cleavage strength of polycrystals”, J. Iron Steel Inst., vol. 174, pp. 25-8 (1953).
19 R.E. Reed-Hill, R. Abbaschian, “Physical Metallurgy Principles”, 3rd ed., PWS-KENT Publishing Company, Boston (1991).
20 E. Malitckii, Y. Yagodzinskyy, H. Hänninen, “Hydrogen charging process instrument”, Fusion Eng. and Design, vol. 100, pp. 142-145 (2015).
21 Y. Yagodzinskyy, O. Todoshchenko, S. Papula, H. Hänninen, “Hydrogen solubility and diffusion in austenitic stainless steels studied with thermal desorption spectroscopy”, Steel Research Int., vol. 82, No 1, pp. 20-25 (2011).
22 C. J. McMahon, M. Cohen, “Initiation of cleavage in polycrystalline iron”, Acta Met., vol. 13, pp. 591-604 (1965).
23 P. Lehto, “Characterization of average grain size and grain size distribution”, Aalto University Wiki, (2016).
24 P. Lehto, J. Romanoff, H. Remes, T. Sarikka, “Characterisation of local grain size variation of welded structural steel”, Weld World, vol. 60, pp. 673-688 (2016).
25 M.Y. Solar, R.I.L. Guthrie, “Hydrogen diffusivities in molten iron between 0.1 and 1.5 atm H_2”, Met. Trans., vol. 2A, pp. 457-64 (1971).
26 R.A. Oriani, “The diffusion and trapping of hydrogen in steels”, Acta Met., vol. 18, pp. 147-157 (1970).
27 K. Ono, L.A. Rosales, “The anomalous behavior of hydrogen in iron at lower temperature”, Trans. Met. Soc., AIME, vol. 242, pp. 244-248 (1968).
28 G.M. Pressouyre, “A classification of hydrogen traps in steel”, Met. Trans., vol. 10A, pp. 1571-1573 (1979).
29 Y.-W. You, X.-S. Kong, X.-B. Wu, Y.-C. Xu, Q.F. Fang, J.L. Chen, G.-N. Luo, C.S. Liu, B.C. Pan, Z. Wang, “Dissolving, trapping and detrapping mechanisms of hydrogen in bcc and fcc transition metals”, J. Appl. Phys., vol. 3, pp. 012118-15 (2013).
30 A. Kimura, H. Kimura, “Hydrogen embrittlement in high purity iron single crystal”, Mater. Sci. Eng., vol. 77, pp. 75-83 (1986).
31 S.P. Lynch, “A fractographic study of gaseous hydrogen embrittlement and liquid-metal embrittlement in a tempered-martensitic steel”, Acta Metall., vol. 32, pp. 79-90 (1984).
32 H.K. Birnbaum, P. Sofronis, “Hydrogen-enhanced localised plasticity – a mechanism for hydrogen-related fracture”, Mater. Sci. Eng., vol. A176, pp. 191-202 (1994).
33 S. Tähtinen, P. Nenonen, H. Hänninen, “Hydrogen-induced microtwinning in ferritic stainless steels”, Scripta Metallurgica, vol. 21, pp. 315-318 (1987).
34 K.T. Kim, J.K. Park, J.Y. Lee, S.H. Hwang, “Effect of alloying elements on hydrogen diffusivity in α-iron”, J. Mat. Sci., vol. 16, pp. 2590-2596 (1981).